

1 Computational single-objective scanning light sheet (cSOLS)

2 Tienan Xu,^{1,2} Hanqi Lin,^{1,2} Yean J Lim,^{1,2} Philip R. Nicovich,³ Katharina Gaus,⁴ And Woei Ming
3 Lee,^{1,2,*}

4 ¹Division of Genomic Sciences and Cancer, The John Curtin School of Medical Research, The Australian
5 National University, Canberra, ACT 2601, Australia

6 ²ACRF INCITe Centre - ANU Node, The John Curtin School of Medical Research, The Australian
7 National University, Canberra, ACT 2601, Australia

8 ³Cajal Neuroscience, 1616 Eastlake Ave E, Seattle, WA 98102, USA

9 ⁴EMBL Australia Node in Single Molecule Science, School of Medical Sciences, University of New
10 South Wales, Sydney, Australia

11 Address for correspondence

12 Dr. W M Lee

13 Division of Genomic Sciences and Cancer,

14 John Curtin School of Medical Research,

15 College of Health and Medicine,

16 The Australian National University,

17 Canberra Act 2601, Australia

18 *Email: steve.lee@anu.edu.au

19

21 **Abstract** Single-objective scanning light sheet (SOLS) imaging has fueled major advances in
22 volumetric bioimaging because it supports low phototoxic, high-resolution imaging over an
23 extended period. The remote imaging unit in SOLS does not use a conventional epifluorescence
24 image detection scheme (a single tube lens). In this paper, we propose a technique called
25 computational SOLS (cSOLS) that achieves light sheet imaging without the remote imaging unit.
26 Using a single microlens array after the tube lens (lightfield imaging), cSOLS is immediately
27 compatible with conventional epifluorescence detection. At the core of cSOLS is a Fast Optical
28 Ray (FOR) model. FOR generates 3D imaging volume ($40 \times 40 \times 14 \mu\text{m}$) using 2D lightfield images
29 taken under SOLS illumination within 0.5 seconds on a standard CPU without multicore parallel
30 processing. In comparison with traditional lightfield retrieval approaches, FOR reassigns
31 fluorescence photons and removes out-of-focus light to improve optical sectioning by a factor of
32 2, thereby achieving a spatial resolution of $1.59 \times 1.92 \times 1.39 \mu\text{m}$. cSOLS with FOR can be tuned
33 over a range of oblique illumination angles and directions, and therefore paves the way for next-
34 generation SOLS imaging. cSOLS marks an important and exciting development of SOLS imaging
35 with instrumental simplicity and computational imaging capabilities.

1 Single-objective scanning light sheet (SOLS) using oblique plane (OP) illumination
 2 techniques have pushed the limits of image-based biological studies such as the quantification of
 3 single-molecule dynamics in living cells [1] to calcium signaling in neuronal circuits in living mice
 4 [2]. All existing single-objective scanning light sheet systems, require costly and more complex
 5 remote imaging units that comprise one or two complementary objective lenses (secondary and
 6 tertiary objective lenses) [3] to achieve diffraction-limited imaging and optical sectioning.
 7 Additional elements such as tailor-made objective lens, tilted mirror, or diffraction grating are
 8 required to effectively image an oblique 3D sample slice on a 2D imaging sensor [4-6]. More
 9 importantly, these remote focusing units are incompatible with conventional epifluorescence
 10 detection paths with a single tube lens and a 2D camera sensor [7]. As such, single-objective
 11 scanning light sheet systems (e.g., eSPIM and SCAPE) are only limited to specialized microscopy
 12 setups [1, 2].

13 Lightfield [8] is a special class of single-shot volumetric fluorescence imaging and is
 14 directly compatible with a standard epifluorescence imaging that leverages computational imaging
 15 that performs 3D depth retrieval using a single 2D lightfield image data. Because of this, lightfield
 16 imaging has been successfully integrated into conventional epifluorescence detection [8, 9].
 17 Lightfield imaging systems have recently reached unprecedented recording speeds under ultra-low
 18 light [10] and highly scattering conditions [9, 11], expanding the imaging field of view into the
 19 millimeter range at single-cell imaging resolution [12]. There are a wide variety of computational
 20 lightfield tools ranging from ray optics interpolation [8], 2) deconvolution iterations [13], to deep
 21 learning reconstruction [14]. All lightfield computational tools are designed to identify 3D
 22 information (x, y, z) of an object based on the angular disparity (r , θ) that is encoded within
 23 lightfield images generated by microlens array (MLA) [8].

24 In conventional epifluorescence detection, 3D sample imaging requires sequential axial
 25 scanning. In a SOLS system, the functional use of a remote imaging unit is to (1) image an oblique
 26 3D sample slice without sequential axial scanning and (2) fulfill the Sine and Hershel conditions
 27 for spherical aberration-free imaging over depth [1]. Fluorescence emitted from an oblique 3D
 28 sample slice is of varying angles along the inclined axial plane [3]. This means that OP lightfield
 29 images alone can readily extract angular disparities of the fluorescence and so retrieve the
 30 respective axial fluorescence points to resolve oblique 3D sample slices without remote imaging

unit or sequential axial scanning. In SOLS, the remote imaging unit fulfills the Sine and Hershel conditions that is no longer matched in cSOLS system because of the use of microlens array. As the result, this tradeoff in cSOLS would operates with a reduced axial imaging range. That said, cSOLS would open up new computational capabilities such as computational adaptive optics to achieve isotropic resolution [10]. In principle, a SOLS system could just require a lightfield imaging unit (a single micro-lens array and a 2D imaging camera) that is fully compatible with conventional epifluorescence detection and replaces the bulky remote imaging unit in SOLS.

However, OP lightfield images present a computational challenge to process using current lightfield depth retrieval tools. Fig. 1 aims to illustrate this challenge. Fig. 1A shows single-objective lens OP illuminating (blue line) over a single 1 μm fluorescence microsphere (red circle) at different angles ($\alpha_1=0^\circ$, $\alpha_2=30^\circ$, $\alpha_3=60^\circ$). Fig. 1B shows corresponding lightfield images. Using lightfield depth retrieval tools [8], we retrieved the point spread function (PSF) from each of the LF images. Fig. 1C shows that the retrieved PSFs from all three distinctively different angles are almost identical. The result shows that the effective imaging PSF ($\text{PSF}_{\text{imaging}}$) is incorrectly represented. This is because $\text{PSF}_{\text{imaging}}$ with an oblique beam is expressed by multiplying OP illumination PSF ($\text{ObliquePSF}_{\text{illumination}}$) with detection PSF ($\text{PSF}_{\text{detection}}$) as shown in Eq. 1 [15].

$$\text{PSF}_{\text{imaging}} = \text{ObliquePSF}_{\text{illumination}} \times \text{PSF}_{\text{detection}} \quad (1)$$

Based on the three different illumination angles, the depth retrieved $\text{PSF}_{\text{imaging}}$, in Fig. 1C, must present a skewed intensity profile [2] (grey ellipse). Because lightfield detection results in a lower spatial resolution compared to the diffraction-limit resolution of the objective lens [13], we anticipate that $\text{PSF}_{\text{detection}}$ has a wider spatial extent than a confined $\text{ObliquePSF}_{\text{illumination}}$ of thin thickness. This means $\text{ObliquePSF}_{\text{illumination}}$ can result in significant spatial modulation over $\text{PSF}_{\text{imaging}}$ in the axial direction through Eq. 1. An incorrect $\text{PSF}_{\text{imaging}}$ would therefore result in inaccuracy in depth retrieval and results in poor Richardson–Lucy deconvolution [16]. It is therefore necessary to restore $\text{PSF}_{\text{imaging}}$. Similar to photon reassignment [17], we proposed that this can be achieved computationally by reassigning fluorescence signal onto an OP illumination plane.

In this Letter, we proposed to build a computational image reassignment model for OP illuminated lightfield systems called Fast Optical Ray (FOR) model. To distinguish FOR model from lightfield depth retrieval methods [8, 13, 14], we term our approach as lightfield depth

1 mapping. FOR model lightfield depth mapping is a ray optics algorithm that rapidly identifies a
 2 3D spatial map of any OP illumination plane. Fluorescence signal from each OP lightfield image
 3 is then computationally mapped into their respective spatial positions in 3D (x, y, z) at 2 planes
 4 per second. The OP illumination is generated using a scanning oblique plane illumination (SOPi)
 5 setup that offers greater flexibility to adjust different OP illumination planes [18]. For lightfield
 6 detection, we constructed a scheme with an unfocused lightfield detection where a microlens array
 7 (MLA) is placed at the image plane of a conventional epi-fluorescence microscope. To ensure
 8 lightfield imaging without overlapping lenslet images, we underfilled each microlens by having
 9 an imaging-side NA smaller than the NA of the MLA (Thorlabs WFS150M-5C). With the 1.3NA
 10 objective lens (Olympus UPLFLN100XOI) used in our system, the maximum oblique angle
 11 achieved in our system is approximately 60° . By limiting the beam diameter using an iris, the OP
 12 illumination possessed an experimentally determined thickness of approximately $1 \mu\text{m}$ at the beam
 13 waist. Details of the system can be found in Supplement S1.

14 Before we introduce the experimental results, we shall first explain the theoretical outline
 15 of FOR model illustrated in Fig. 2A. FOR model uses ray transfer matrix analysis, where
 16 individual rays of a voxel V are mapped from the object space to the sensor plane S as shown in
 17 Eq. 2 below,

$$18 \quad S_{x,y}(N) = [P][L_{MLA}][P][L_{tube}][P][L_{obj}]V_{x,y,z,x',y'}(N) \quad (2)$$

19 where the voxel's spatial coordinates are x, y, z , rays emitted from the voxel are indexed
 20 by N , a ray's coordinates on the aperture of the objective lens are given by x', y' , a ray's
 21 coordinates on the sensor plane are x, y , the free space transfer term is $[P]$, and the thin lens
 22 transfer terms for the objective lens, tube lens, and MLA are defined as $[L_{obj}]$, $[L_{tube}]$, and $[L_{MLA}]$,
 23 respectively. FOR model performs 4x4 ray transfer analysis to model XZ and YZ propagations of
 24 rays from a voxel V to the sensor plane S . We model XZ and YZ propagations separately using
 25 two sets of 2x2 ray transfer matrices. The results are then combined to express a ray's 2D
 26 divergence angles from the optical axis. For simplicity, Fig. 2A illustrates the XZ propagation
 27 paths and ray transfer terms. V is formed by discrete sampling of the object space using lateral and
 28 axial sampling factors δxy and δz . δxy and δz together represent the smallest voxel in the object
 29 space that FOR model can analyze. Using the focal point of the objective lens as the origin, a
 30 dataset consisting of voxels V in the object space with spatial coordinates x, y, z (multiples of δxy

1 and δz) relative to the focal point is generated. By evenly distributing N rays emitted from the
 2 voxel V on the aperture of the objective lens with spatial coordinates x', y' where the rays enter
 3 the imaging system from different angles, FOR model samples the angular information of signal
 4 from the voxel V . By indexing each unique ray with N , $S(N)$ represents the lateral coordinates of
 5 the ray $V(N)$ on the sensor plane.

6 In Fig. 2A, we showed an OP (blue line, denoted by K_2) that is detected on the imaging
 7 sensor after the MLA. Next, we determine the expected pixels that would create the following
 8 lightfield image. Eq. 3 describes how the sensor plane S is mapped to the lightfield image LF,

$$9 \quad LF_{l,m}(N) = S_{x,y}(N)/U \quad (3)$$

10 where the sensor's pixel size is U , and lightfield image pixel coordinates are l, m . For illustration
 11 purpose, Fig. 2A shows four light rays $V(1)$ to $V(4)$ that are focused through the MLA onto the
 12 camera sensor at $S(1)$ to $S(4)$ and recorded as $LF(1)$ to $LF(4)$. We then used Eq. 4 to calculate
 13 the expected intensity of the respective voxel.

$$14 \quad I_{x,y,z} = \frac{1}{N} \sum_1^N LF_{l,m}(N) \quad (4)$$

15 The detected intensity I is the summation and averaging of all rays $V(1)$ to $V(4)$. Since a
 16 camera sensor samples an image discretely, bilinear interpolation is applied at this step to construct
 17 each voxel intensities. Fig. 2B illustrates how FOR model maps OP illumination in object space
 18 to form a volumetric image. Fig. 2B i) shows diagonally tilted voxels across a single volume that
 19 are excited by three OP illumination slices (K_1, K_2, K_3). FOR model identifies the illumination
 20 slice which is then used to determine the corresponding fluorescence intensities (details in
 21 Supplement S2). Fig. 2B ii) shows that the chosen fluorescence intensities are then rearranged in
 22 separate columns of pixels. For a given illumination slice, we plot the respective OP images P
 23 shown as P_1, P_2, P_3 in Fig. 2B ii). Oblique fluorescence intensities are then mathematically
 24 reassigned back into the 3D positions in 4 different Z-slices as shown in Fig. 2B iii). The
 25 reassignment process is given in Eq. 5,

$$26 \quad Z_z = P_{k(z)} \quad (5)$$

1 where $P_{k(z)}$ is the set of OP images, and Z_z is the slice at depth z . Both OP images and Z-slices
 2 have pixel coordinates i, j . $k(z)$ is described in Supplement S2 which are used to locate the OP
 3 image with index k where pixel i, j is to be extracted from.

4 To fulfill the Nyquist sampling criterion in our discrete FOR model, we set δxy and δz as
 5 $0.25 \mu\text{m}$ and $0.5 \mu\text{m}$, which are more than 4 times smaller than the theoretical lateral and axial
 6 resolution $1.35 \mu\text{m}$ and $2.16 \mu\text{m}$ of our lightfield detection (details in Supplement S1). FOR model
 7 with fine lateral and axial sampling allows accurate determination of $S_{x,y}$ and therefore $I_{x,y,z}$.
 8 Details on the impact of sampling density on FOR model depth mapping can be found in
 9 Supplement S3. Current implementation of FOR model utilizes paraxial ray transfer matrix
 10 analysis and therefore is subject to propagation inaccuracies. However, this allows FOR model to
 11 be highly efficient and adaptive to different optics including objective lenses and MLAs as paraxial
 12 thin lens modeling does not rely on the detailed parameters of optics (e.g., refractive index, surface
 13 curvature, thickness). To optimize for speed, we pre-compute FOR model to generate a dataset of
 14 $S_{x,y}$ of the lightfield detection. $S_{x,y}$ applies to all lightfield images captured for different samples.
 15 This allows real-time depth mapping and image reassignment to be performed in MATLAB at 2
 16 OP lightfield images per second. For imaging a volume of $40 \times 40 \times 14 \mu\text{m}$ with 60° OP illumination
 17 that is captured with 50 OP illuminated lightfields, current CPU-based (AMD Ryzen 7 5800X,
 18 32GB RAM, non-parallel processing) achieves FOR model depth mapping in 25 seconds. This
 19 could be shortened by 25 times after implementing multicore parallel processing, achieving full
 20 3D depth mapping at 1 volume per second. In comparison, for the same imaging volume and the
 21 number of lightfields, lightfield depth retrieval based on deconvolution iteration [13] takes ~40
 22 minutes to compute (Supplementary S6). We anticipate that deep learning-based lightfield
 23 methods can achieve multiple volumes per second, however, requires a sophisticated model
 24 training and validation process [14]. Computational considerations of FOR model generation and
 25 real-time depth mapping are summarized in Supplementary S4.

26 Next, we experimentally validate FOR model depth mapping for an OP illumination angle
 27 of 60° and compare it against lightfield depth retrieval based on ray optics [8]. We used $1 \mu\text{m}$
 28 diameter fluorescence microspheres (Polysciences Fluoresbrite YG Microspheres) that are below
 29 the resolution limit of the optical system. Supplement S5 outlines FOR model parameters used for
 30 processing. Fig. 3A shows the $1 \mu\text{m}$ microsphere retrieved without FOR model depth mapping

1 showing a significant amount of out-of-focus blur in both XZ and YZ planes. However, the same
 2 microsphere processed by FOR model depth mapping demonstrates a greatly reduced out-of-focus
 3 signal by 2 folds in the vertical direction as shown in Fig. 3B and Fig. 4. Using FOR model depth
 4 mapping, we acquired the effective $\text{PSF}_{\text{imaging}}$ with vertical FWHMs ($1.39\ \mu\text{m}$ and $1.37\ \mu\text{m}$) in XZ
 5 and YZ that are close to the theoretical limit of the system which is $1.35\ \mu\text{m}$ with a profile almost
 6 identical to the ideal $\text{PSF}_{\text{imaging}}$ and in doing so achieves accurate depth sectioning of the
 7 microsphere. In Fig. 3C, while lightfield depth retrieval and FOR model depth mapping
 8 demonstrate comparable XY FWHMs of $1.94\ \mu\text{m}$ and $1.92\ \mu\text{m}$ in the vertical direction, the
 9 effective $\text{PSF}_{\text{imaging}}$ acquired by FOR model depth mapping shows an asymmetry profile in the
 10 lateral direction of $1.59\ \mu\text{m}$. Noting that the asymmetry is aligned with the OP illumination sample
 11 scan direction in the lateral axis, it is possibly an artifact associated with the sample scanning or
 12 data interpolation. We anticipate that this artifact can be resolved by OP illumination sample scan
 13 at finer steps and improved interpolation strategy (e.g., cubic interpolation) during FOR model
 14 depth mapping and image reassignment.

15 To further validate our model on densely packed samples, we performed imaging on
 16 customized laser-written rigid fluorescence microstructure, illustrated in Fig. 5A (not drawn to
 17 scale). Using multiphoton lithography, we constructed a microstructure consisting of letters “A”
 18 (red) and “U” (blue) stacked vertically on a glass coverslip and by supporting structures (green).
 19 The 3D fabrication process is described in Supplement S8. For comparison, we performed
 20 deconvolution on images acquired by FOR model depth mapping using the captured $\text{PSF}_{\text{imaging}}$ and
 21 compared with a lightfield depth retrieval method based on wave optics deconvolution iteration
 22 [13]. Parameters for lightfield deconvolution can be found in Supplementary S6. Fig. 5B shows
 23 XY slices containing letters “A” and “U” at $z = -2\ \mu\text{m}$ and $z = 2\ \mu\text{m}$, respectively. This gives a
 24 small separation of $4\ \mu\text{m}$ along the z axis between “A” and “U” to test axial sectioning. From Fig.
 25 5B, both lightfield depth retrieval and FOR model depth mapping appear to show the letters at
 26 their designated axial position accurately, excluding any out-of-focus intensity arising from the
 27 other letter located $4\ \mu\text{m}$ away in z . However, upon closer examination of the YZ slice (Fig. 5C)
 28 across the center of the microstructure (blue dashed plane in Fig. 5A), we observed that lightfield
 29 depth retrieval, Fig. 5C i), only eliminated half of the out-of-focus cones, while depth mapping,
 30 Fig. 5C ii), shows no out-of-focus cones. Fig. 5D plots the normalized axial intensity across the
 31 letter “A” (white lines in Fig. 5C) and quantifies the out-of-focus region. We found that lightfield

1 depth retrieval results in an out-of-focus region extending over $8\ \mu\text{m}$ (FWHM) in depth.
 2 Conversely, FOR model depth mapping achieves accurately mapped to $z = -2\ \mu\text{m}$ with an axial
 3 profile (FWHM) of $1.9\ \mu\text{m}$ resulting in sharp axial fluorescence signal of the letter “A”. The results
 4 of FOR model depth mapping on densely packed fluorescence microstructures show significant
 5 improvement in depth sectioning over lightfield depth retrieval, as shown in Fig. 6. However,
 6 observed in Fig. 5B qualitatively that FOR model depth mapping demonstrates inferior lateral
 7 resolvability of the microstructure to the lightfield depth retrieval method.

8 In conclusion, we demonstrated a novel computational single-objective scanning light
 9 sheet (cSOLS) imaging technique enabled by our FOR model depth mapping lightfield algorithm.
 10 With the remote imaging unit removed, FOR model depth mapping allows SOLS imaging to be
 11 performed on conventional epifluorescence detection scheme. This immediately promotes single-
 12 objective scanning light sheet imaging in potential clinical applications with handheld devices of
 13 simplified optical designs [19]. cSOLS with FOR can be integrated into a wide range of existing
 14 high throughput imaging systems for high contents screening with the addition of a new OP
 15 illumination module. We also confirmed that conventional lightfield depth retrieval methods fail
 16 to retrieve OP illuminated images. FOR model depth mapping achieves an effective $\text{PSF}_{\text{imaging}}$ with
 17 axial FWHMs ($1.39\ \mu\text{m}$ and $1.37\ \mu\text{m}$) that are close to the lateral resolution limit ($1.35\ \mu\text{m}$) of our
 18 lightfield detection [8]. Shown in Table 1, cSOLS with FOR achieved spatial resolution that is
 19 comparable to existing single-objective light sheet systems of comparable effective NA [20, 21].
 20 We anticipate that the enhancement of optical sectioning achieved by FOR model depth mapping
 21 can immediately benefit high-contrast imaging of live developing zebrafishes [16]. FOR model
 22 depth mapping achieves optical sectioning on densely packed structures that existing lightfield
 23 algorithms cannot [22]. By adopting MLA-based lightfield detection, SOLS imaging can benefit
 24 from technological advances in lightfield computational imaging. cSOLS with FOR can be further
 25 tailored to structured OP beam such as Airy beam light sheet for potential large FOV, high-contrast
 26 imaging with improved resistance to scattering in biological samples [23]. Implementing two-
 27 photon light sheet can also improve depth penetration when imaging thick biological samples.
 28 cSOLS with FOR has the potential to adopt computational adaptive optics for aberration correction
 29 without “guide star” or additional wavefront sensing and in turn promises imaging deep inside
 30 samples [10]. FOR model can also accommodate multidimensional OP illuminated lightfield
 31 spectral imaging [24], and is able to computationally resolve multi-direction OP illumination for

This is the author's peer reviewed, accepted manuscript. However, the online version of record will be different from this version once it has been copyedited and typeset.

PLEASE CITE THIS ARTICLE AS DOI:10.1063/5.0091615

multi-view light sheet imaging for highly scattering samples [25]. A key area of improvement in FOR model is the remaining 7.5% mismatch between $\text{ObliquePSF}_{\text{illumination}}$ and $\text{PSF}_{\text{detection}}$ due to experimental uncertainty in determining oblique angles, which can be improved using additional calibration steps [18]. Furthermore, current FOR model depth mapping requires prior manual calibration of the illumination profile for effective optical sectioning. This calibration process can be automated by performing wavefront sensing of the illumination at the back focal plane of the objective lens. Current implementation of FOR model depth mapping considers OP illuminations of a uniform thickness for simplicity, which is not a realistic model as Gaussian beam diverges in regions outside of the beam waist. The effect of beam divergence could be addressed in FOR model by incorporating variable OP illumination thickness as a next step when adopting a large FOV. Here, we validated cSOLS with FOR to have a spatial resolution of $1.59 \times 1.92 \times 1.39 \mu\text{m}$ over an imaging depth range of $14 \mu\text{m}$, which is lower than traditional SOLS that uses remote focusing unit to satisfy the Sine condition (Supplementary S7). The limited imaging depth is because of the focusing properties of MLA. Recent advance in liquid crystal MLA with tunable focusing and numerical aperture can improve the imaging depth of cSOLS [26]. cSOLS with FOR also has anisotropic spatial resolution across depth, which is a factor inherent to lightfield imaging [9, 13]. This can be overcome by complete space multiscale lightfield modelling [9] and computational adaptive optics [10] to achieve FOR cSOLS imaging with aberration correction and isotropic resolution. We anticipate that FOR model depth mapping will adopt these computational methods to extend the imaging depth to $180 \mu\text{m}$. Although the spatial resolution of cSOLS with FOR is around half of high-NA SOLS systems [4], this can be overcome by adopting scanning lightfield techniques [10] or Fourier lightfield detection [27] to reach $\sim 300 \text{ nm}$ laterally and $\sim 700 \text{ nm}$ axially that are comparable to both high-NA SOLS and orthogonal light sheet systems. An important future step for FOR model is to adopt wave optics-based propagation and deconvolution to minimize propagation inaccuracy, increase spatial resolution, and increase signal-to-noise ratio. MLA-based lightfield detection is subject to the tradeoff between spatial resolution and depth resolvability which ultimately limits biological imaging capabilities. This can be alleviated by adopting MLA and camera with finer pitch and pixel size. We envision that cSOLS using MLA with tunable optical properties [28] and computational adaptive optics [10] will reach subcellular imaging resolution with improve depth resolvability. Recent CUDA processing will also accelerate FOR model depth mapping volume rate to up to 30 volumes per second [8, 29]. Finally, we expect

1 FOR model to complement existing lightfield deep-learning methods to reach sub-cellular imaging
2 resolution with simplified signal processing pipelines and at hundreds of volumes per second [14].

3

4 **Supplementary Material.** See supplementary material for detailed methods. Supplementary S1
5 describes details on optical system. Supplementary S2 describes modeling of scanned oblique
6 plane illumination in FOR model. Supplementary S3 shows impact of sampling on FOR model
7 depth mapping performance. Supplementary S4 outlines computational consideration of FOR
8 model depth mapping. Supplementary S5 summarizes FOR model depth mapping parameters for
9 experimental data processing. Supplementary S6 describes parameters for lightfield deconvolution.
10 Supplementary S7 shows resolution and imaging depth comparison with SOLS approaches.
11 Supplementary S8 describes the multiphoton lithography fabrication process.

12 **Funding.** Australian Research Council (DE160100843, DP190100039, DP200100364.
13 CE140100011).

14 **Acknowledgement.** Katharina Gaus is deceased.

15 **Disclosures.** W.M.L. and T.X. have filed a Patent.

16 **Data availability.** The data that support the findings of this study are available from the
17 corresponding author upon reasonable request.

Figure 1

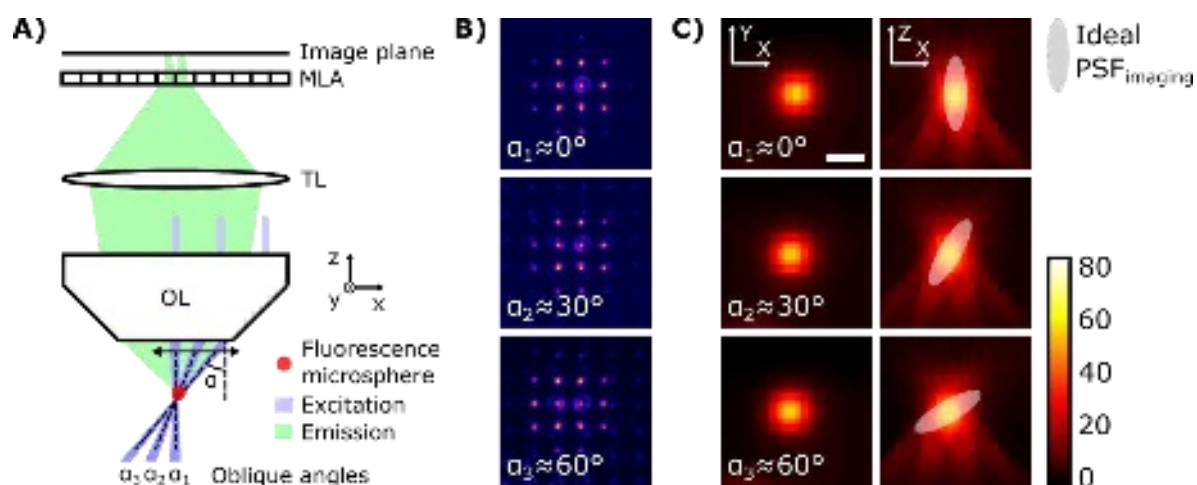


Fig. 1. A) An illustration showing lightfield imaging of a sub-resolution fluorescence sample under OP illumination of different angles ($\alpha_1=0^\circ$, $\alpha_2=30^\circ$, $\alpha_3=60^\circ$). B) Lightfield images captured for the three illumination conditions. C) Transverse (XY) and axial (XZ) PSF_{imaging} retrieved from lightfield images using a lightfield depth retrieval tool. Grey eclipses show the ideal PSF_{imaging} corresponding to OP illumination of different angles. Scale bar: 2 μm .

This is the author's peer reviewed, accepted manuscript. However, the online version of record will be different from this version once it has been copyedited and typeset.

PLEASE CITE THIS ARTICLE AS DOI:10.1063/5.0091615

Figure 2

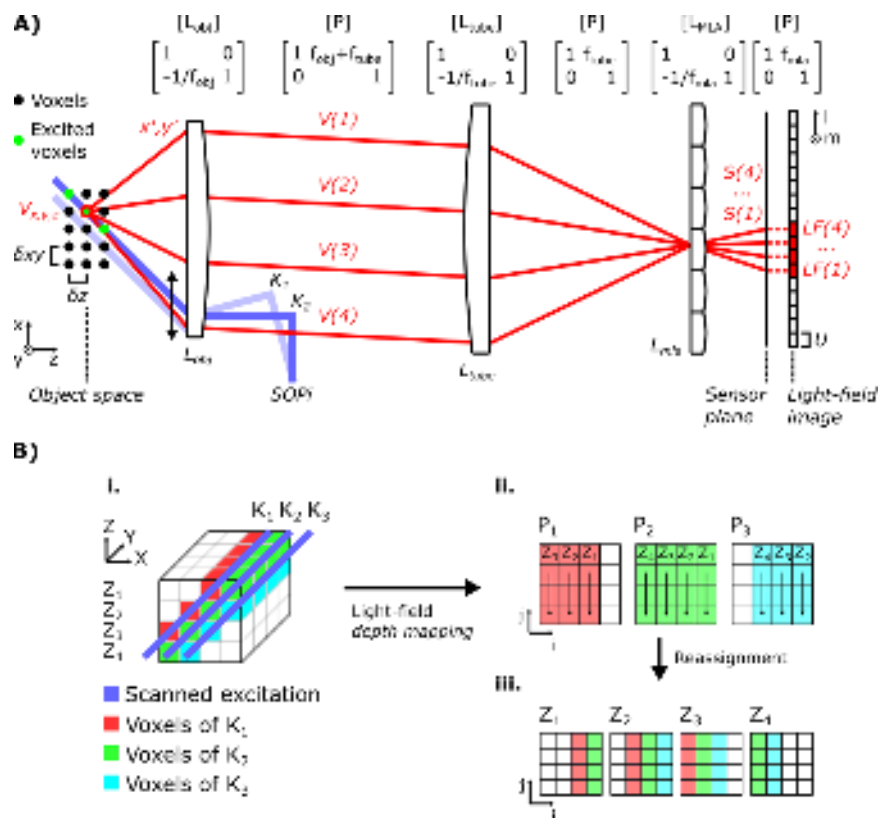


Fig. 2. A) A schematic of FOR model showing a voxel $V_{x,y,z}$ with four light rays $V(1) \sim V(4)$ traced from the object space to coordinates $S(1) \sim S(4)$ on the sensor plane, then mapped to pixels $LF(1) \sim LF(4)$ of a lightfield image. K_1 and K_2 denote OP illumination slices. B) (i) A schematic showing FOR model depth mapping extracts excited voxels from OP illumination slices K_1 to K_3 to form (ii). OP images P_1 and P_3 . (iii) Reassignment is applied to convert OP images to a Z-stack containing slices Z_1 and Z_4 .

Figure 3

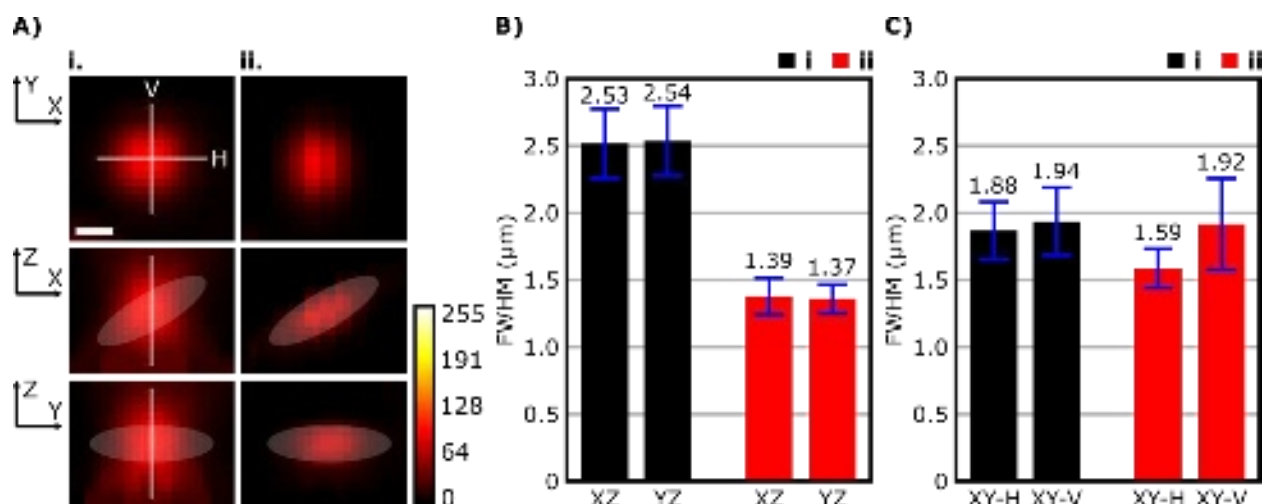
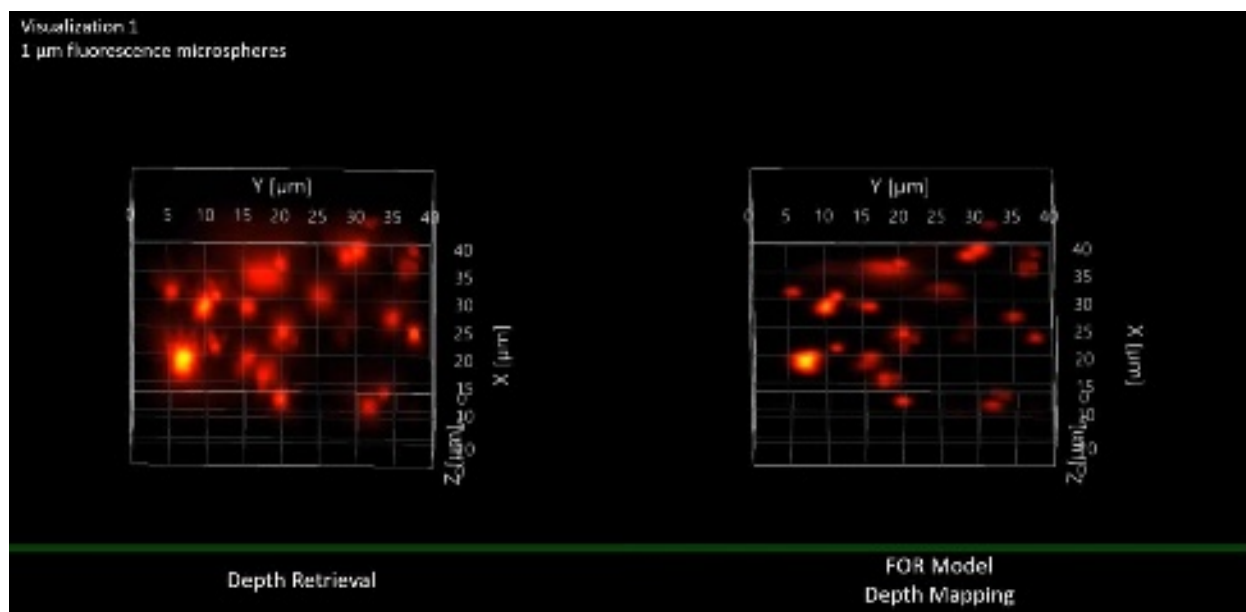


Fig. 3. A) XY, XZ, and YZ slices of a 1 μm fluorescent microsphere excited by scanned OP illumination at 60° and retrieved by (i) – lightfield depth retrieval and (ii) – FOR model depth mapping. Grey eclipses show the ideal PSF_{imaging}. White lines are for axial FWHM measurements. Scale bar: 1 μm . B) Bar plots of XZ and YZ vertical FWHM profiles of the 1 μm fluorescent microsphere. C) Bar plots of XY FWHM profiles (both lateral and vertical) of the 1 μm fluorescent microsphere. Error bars are shown in blue. Data are mean values and standard deviations of five 1 μm fluorescent microspheres.

This is the author's peer reviewed, accepted manuscript. However, the online version of record will be different from this version once it has been copyedited and typeset.
PLEASE CITE THIS ARTICLE AS DOI:10.1063/5.0091615

1 **Figure 4**

2



3

4 Fig. 4. 1 μm fluorescent microspheres excited by scanned OP illumination at 60° and retrieved by
5 (left) – lightfield depth retrieval and (right) – FOR model depth mapping. (Multimedia view)

Figure 5

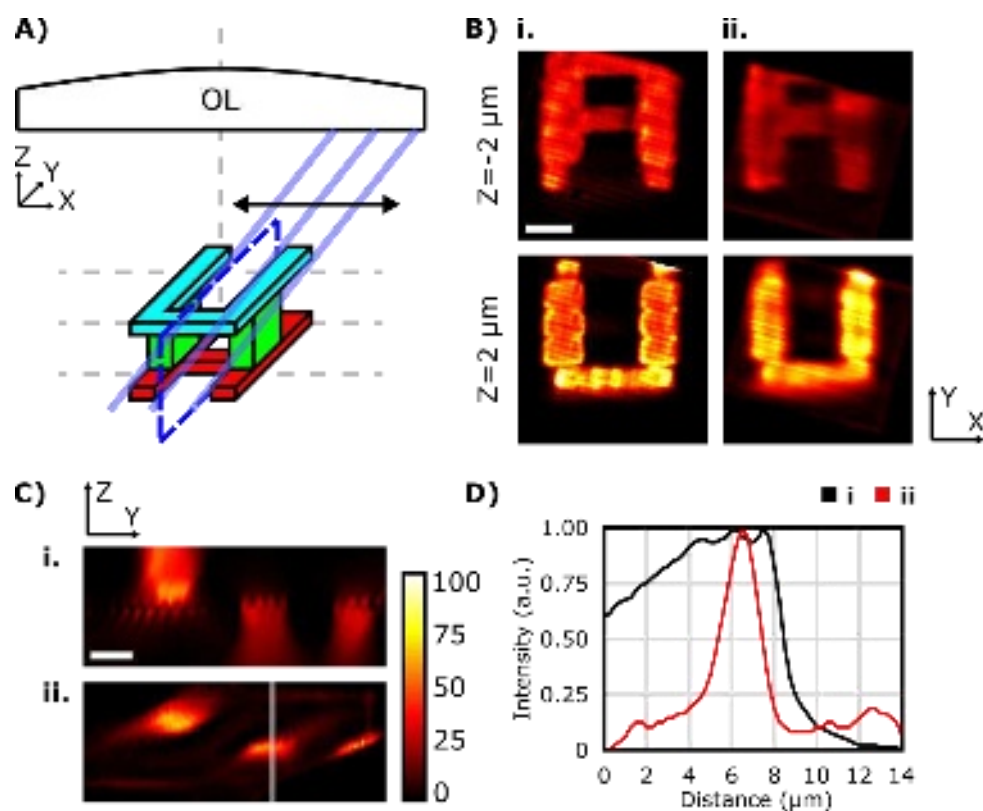
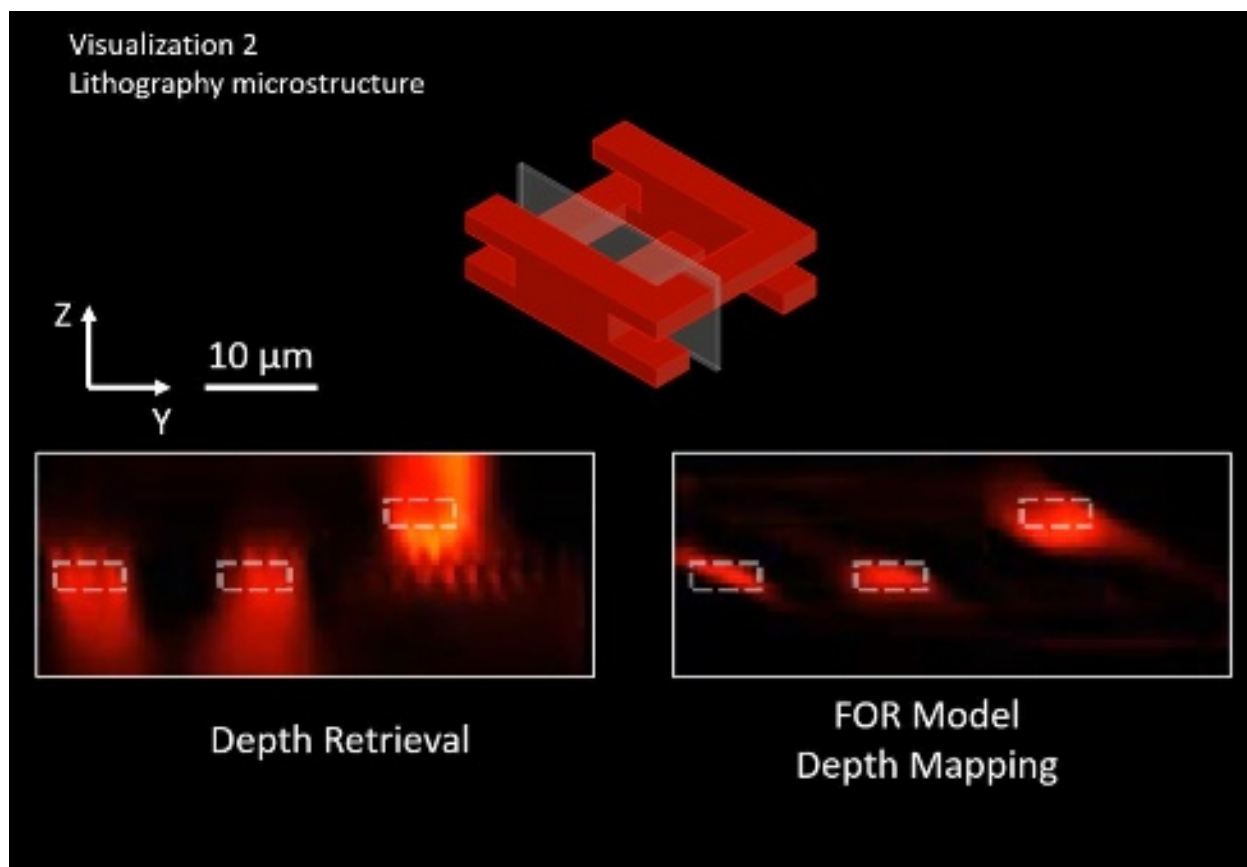


Fig. 5. A) A schematic demonstrating imaging of the lithographic microstructure. Solid blue lines represent scanned OP illumination. Dashed blue lines represent the YZ slice across the center of the microstructure. B) XY slices containing letters “A” and “U” at $z = -2 \mu\text{m}$ and $z = 2 \mu\text{m}$ retrieved by (i) lightfield depth retrieval and (ii) FOR model depth mapping. Scale bar: 10 μm . C) YZ slices across the center of the microstructure. Scale bar: 5 μm . D) Normalized axial intensity profiles across letter “A”.

1 **Figure 6**

2



3

4 Fig. 6. YZ slices across the center of the microstructure retrieved by (left) – lightfield depth
5 retrieval and (right) – FOR model depth mapping. (Multimedia view)

1 **Table 1**

2

	SCAPE 2.0 [21]		1P SOPI [20]	cSOLS with FOR
Detection	Remote imaging unit		Remote imaging unit	Lightfield
Objective lens	Olympus XLUMPLFLN 20x/1.0NA W		Olympus XLUMPLFLN 20x/1.0NA W	Olympus UPLFLN 100x/1.3NA Oil
	Nikon CFI Plan Apo Lambda 20x/0.75NA		Olympus UPLSAPO 20x/0.75NA	
	EO HR 20x/0.60NA	Nikon Plan Apo HR 50x/0.75NA	Olympus LUCPLFLN 20x/0.45NA	
Effective detection NA	0.23	0.35	0.34	0.235
X (μm)	1.47	1.21	1.30 (axis not specified)	1.59
Y (μm)	0.86	0.60		1.92
Z (μm)	1.96	1.55		1.39

3

4 Table 1. Spatial resolution comparison of SOLS approaches

References

1. B. Yang, X. Chen, Y. Wang, S. Feng, V. Pessino, N. Stuurman, N. H. Cho, K. W. Cheng, S. J. Lord, L. Xu, D. Xie, R. D. Mullins, M. D. Leonetti, and B. Huang, *Nature Methods* **16**, 501-504 (2019).
2. M. B. Bouchard, V. Voleti, C. S. Mendes, C. Lacefield, W. B. Grueber, R. S. Mann, R. M. Bruno, and E. M. C. Hillman, *Nature Photonics* **9**, 113-119 (2015).
3. C. Dunsby, *Opt. Express* **16**, 20306-20316 (2008).
4. E. Sapoznik, B.-J. Chang, J. Huh, R. J. Ju, E. V. Azarova, T. Pohlkamp, E. S. Welf, D. Broadbent, A. F. Carisey, S. J. Stehbins, K.-M. Lee, A. Marín, A. B. Hanker, J. C. Schmidt, C. L. Arteaga, B. Yang, Y. Kobayashi, P. R. Tata, R. Kruithoff, K. Doubrovinski, D. P. Shepherd, A. Millett-Sikking, A. G. York, K. M. Dean, and R. P. Fiolka, *eLife* **9**, e57681 (2020).
5. J. Kim, M. Wojcik, Y. Wang, S. Moon, E. A. Zin, N. Marnani, Z. L. Newman, J. G. Flannery, K. Xu, and X. Zhang, *Nature Methods* **16**, 853-857 (2019).
6. M. Hoffmann, and B. Judkewitz, *Optica* **6**, 1166-1170 (2019).
7. R. Fiolka, *Nature Methods* **16**, 813-814 (2019).
8. M. Levoy, Z. Zhang, and I. McDowall, *Journal of Microscopy* **235**, 144-162 (2009).
9. Y. Zhang, Z. Lu, J. Wu, X. Lin, D. Jiang, Y. Cai, J. Xie, Y. Wang, T. Zhu, X. Ji, and Q. Dai, *Nature Communications* **12**, 6391 (2021).
10. J. Wu, Z. Lu, D. Jiang, Y. Guo, H. Qiao, Y. Zhang, T. Zhu, Y. Cai, X. Zhang, K. Zhanghao, H. Xie, T. Yan, G. Zhang, X. Li, Z. Jiang, X. Lin, L. Fang, B. Zhou, P. Xi, J. Fan, L. Yu, and Q. Dai, *Cell* **184**, 3318-3332.e3317 (2021).
11. Y. Zhang, B. Xiong, Y. Zhang, Z. Lu, J. Wu, and Q. Dai, *Light: Science & Applications* **10**, 152 (2021).
12. Y. Xue, I. G. Davison, D. A. Boas, and L. Tian, *Science Advances* **6**, eabb7508 (2020).
13. M. Broxton, L. Grosenick, S. Yang, N. Cohen, A. Andalman, K. Deisseroth, and M. Levoy, *Opt. Express* **21**, 25418-25439 (2013).
14. Z. Wang, L. Zhu, H. Zhang, G. Li, C. Yi, Y. Li, Y. Yang, Y. Ding, M. Zhen, S. Gao, T. K. Hsiai, and P. Fei, *Nature Methods* **18**, 551-556 (2021).
15. K. Becker, S. Saghafi, M. Pende, I. Sabyusheva-Litschauer, C. M. Hahn, M. Foroughipour, N. Jährling, and H.-U. Dodt, *Scientific Reports* **9**, 17625 (2019).
16. S. Madaan, K. Keomanee-Dizon, M. Jones, C. Zhong, A. Nadtochiy, P. Luu, S. E. Fraser, and T. V. Truong, *Opt. Lett.* **46**, 2860-2863 (2021).
17. C. J. R. Sheppard, M. Castello, G. Tortarolo, T. Deguchi, S. V. Koho, G. Vicidomini, and A. Diaspro, *J. Opt. Soc. Am. A* **37**, 154-162 (2020).
18. M. Kumar, and Y. Kozorovitskiy, *Biomed. Opt. Express* **11**, 3346-3359 (2020).
19. K. B. Patel, W. Liang, M. J. Casper, V. Voleti, W. Li, A. J. Yagielski, H. T. Zhao, C. Perez Campos, G. S. Lee, J. M. Liu, E. Philipone, A. J. Yoon, K. P. Olive, S. M. Coley, and E. M. C. Hillman, *Nature Biomedical Engineering* (2022).
20. M. Kumar, S. Kishore, J. Nasenbeny, D. L. McLean, and Y. Kozorovitskiy, *Opt. Express* **26**, 13027-13041 (2018).
21. V. Voleti, K. B. Patel, W. Li, C. Perez Campos, S. Bharadwaj, H. Yu, C. Ford, M. J. Casper, R. W. Yan, W. Liang, C. Wen, K. D. Kimura, K. L. Targoff, and E. M. C. Hillman, *Nature Methods* **16**, 1054-1062 (2019).
22. E. Sánchez-Ortiga, G. Scrofani, G. Saavedra, and M. Martinez-Corral, *IEEE Access* **8**, 14944-14952 (2020).
23. T. Vettenburg, H. I. C. Dalgarno, J. Nytk, C. Coll-Lladó, D. E. K. Ferrier, T. Čížmár, F. J. Gunn-Moore, and K. Dholakia, *Nature Methods* **11**, 541-544 (2014).

This is the author's peer reviewed, accepted manuscript. However, the online version of record will be different from this version once it has been copyedited and typeset.

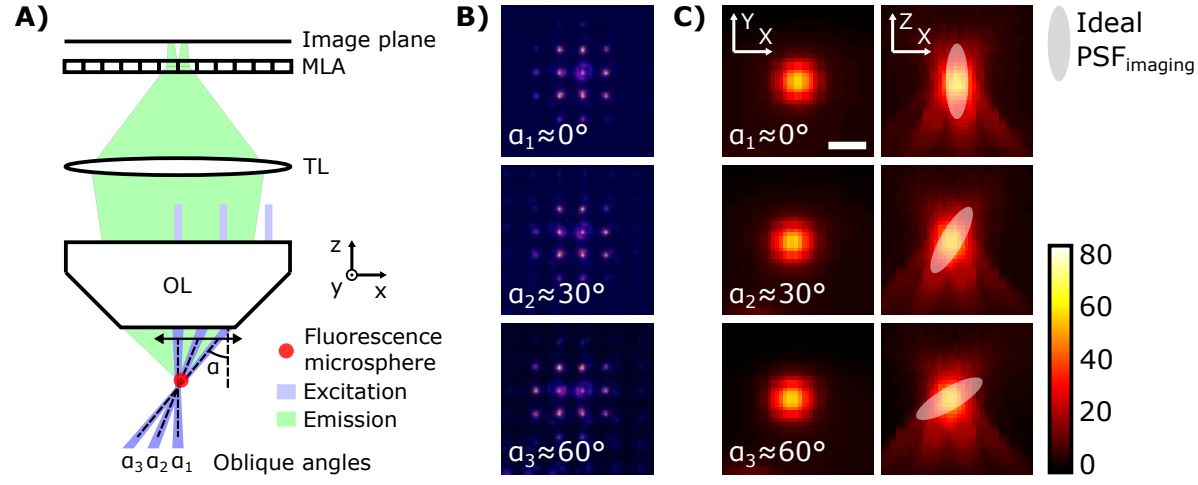
PLEASE CITE THIS ARTICLE AS DOI:10.1063/5.0091615

- 1 24. J. Park, X. Feng, R. Liang, and L. Gao, *Nature Communications* **11**, 5602 (2020).
- 2 25. B. Yang, M. Lange, A. Millett-Sikking, X. Zhao, J. Bragantini, S. VijayKumar, M. Kamb, R. Gómez-
- 3 Sjöberg, A. C. Solak, W. Wang, H. Kobayashi, M. N. McCarroll, L. W. Whitehead, R. P. Fiolka, T. B.
- 4 Kornberg, A. G. York, and L. A. Royer, *Nature Methods* **19**, 461-469 (2022).
- 5 26. J. F. Algorri, N. Bennis, V. Urruchi, P. Morawiak, J. M. Sánchez-Pena, and L. R. Jaroszewicz,
- 6 *Scientific Reports* **7**, 17318 (2017).
- 7 27. H. Li, C. Guo, D. Kim-Holzappel, W. Li, Y. Altshuller, B. Schroeder, W. Liu, Y. Meng, J. B. French, K.-
- 8 I. Takamaru, M. A. Frohman, and S. Jia, *Biomed. Opt. Express* **10**, 29-49 (2019).
- 9 28. N. Chronis, G. L. Liu, K.-H. Jeong, and L. P. Lee, *Opt. Express* **11**, 2370-2378 (2003).
- 10 29. M. Guo, Y. Li, Y. Su, T. Lambert, D. D. Nogare, M. W. Moyle, L. H. Duncan, R. Ikegami, A. Santella,
- 11 I. Rey-Suarez, D. Green, A. Beiriger, J. Chen, H. Vishwasrao, S. Ganesan, V. Prince, J. C. Waters, C. M.
- 12 Annunziata, M. Hafner, W. A. Mohler, A. B. Chitnis, A. Upadhyaya, T. B. Usdin, Z. Bao, D. Colón-Ramos, P.
- 13 La Riviere, H. Liu, Y. Wu, and H. Shroff, *Nature Biotechnology* **38**, 1337-1346 (2020).

14

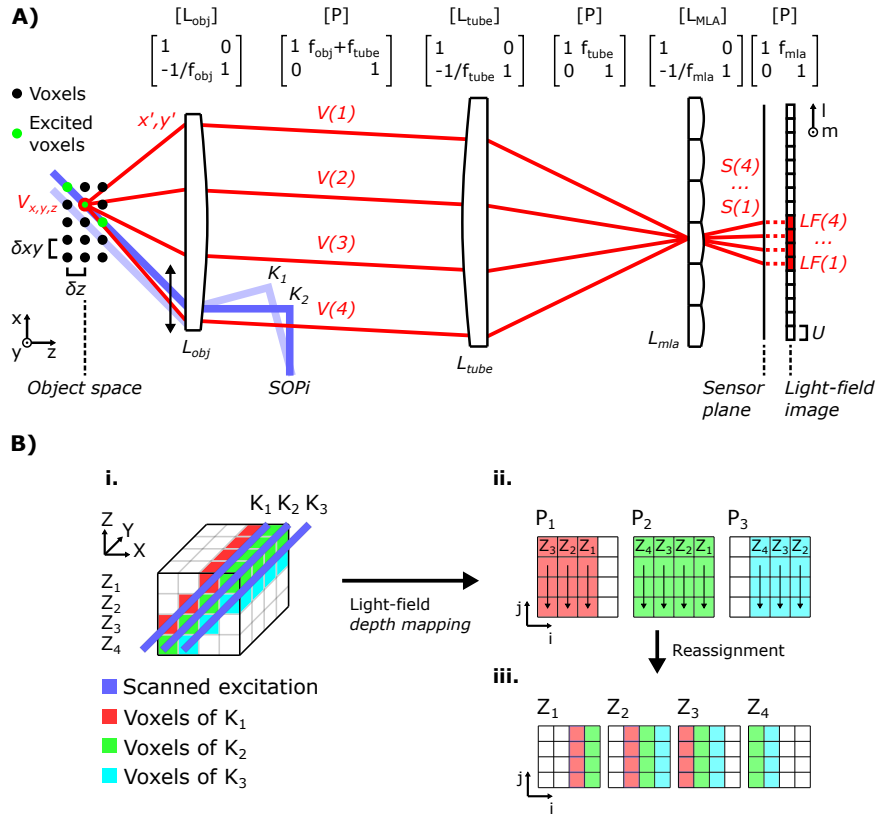
This is the author's peer reviewed, accepted manuscript. However, the online version of record will be different from this version once it has been copyedited and typeset.

PLEASE CITE THIS ARTICLE AS DOI:10.1063/5.0091615



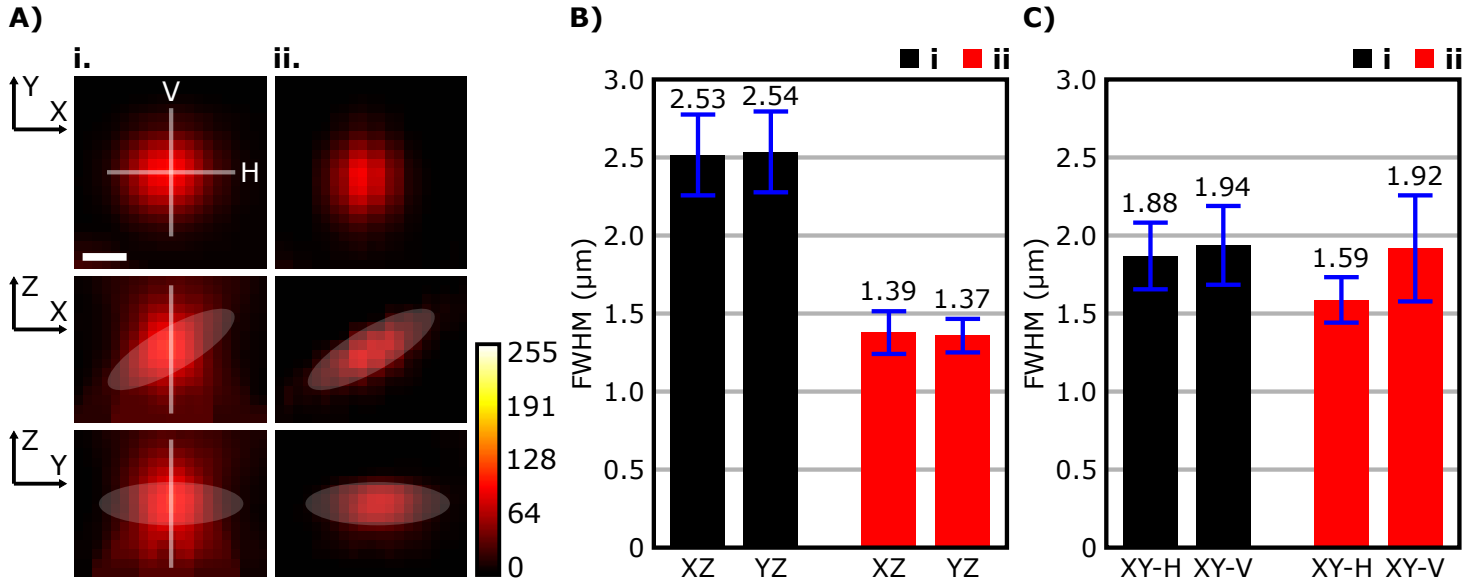
This is the author's peer reviewed, accepted manuscript. However, the online version of record will be different from this version once it has been copyedited and typeset.

PLEASE CITE THIS ARTICLE AS DOI:10.1063/5.0091615

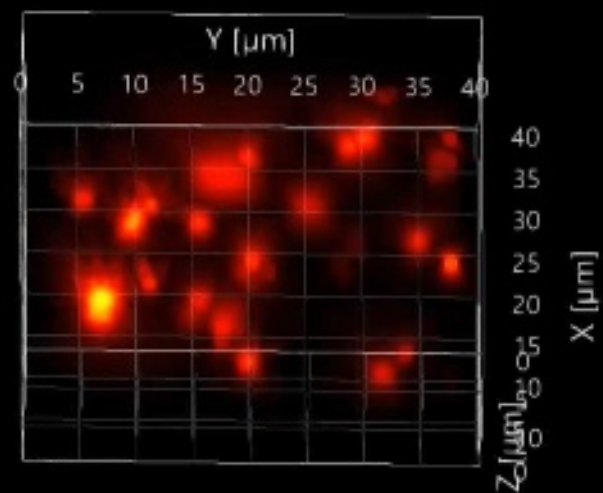


This is the author's peer reviewed, accepted manuscript. However, the online version of record will be different from this version once it has been copyedited and typeset.

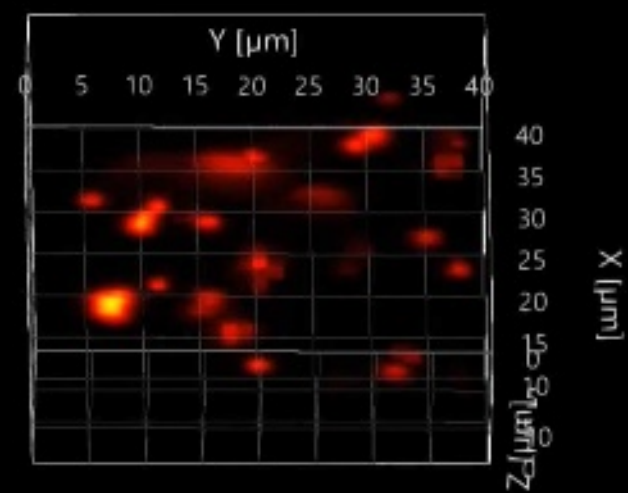
PLEASE CITE THIS ARTICLE AS DOI:10.1063/5.0091615



Visualization 1

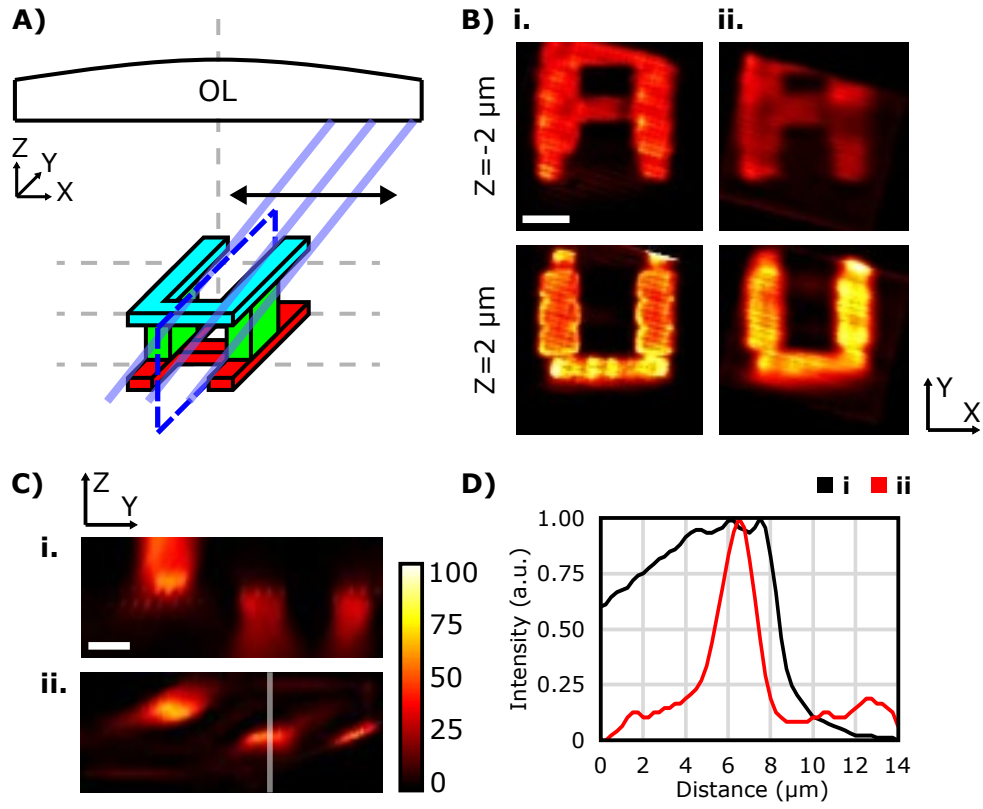
 $1\text{ }\mu\text{m}$ fluorescence microspheres

Depth Retrieval

FOR Model
Depth Mapping

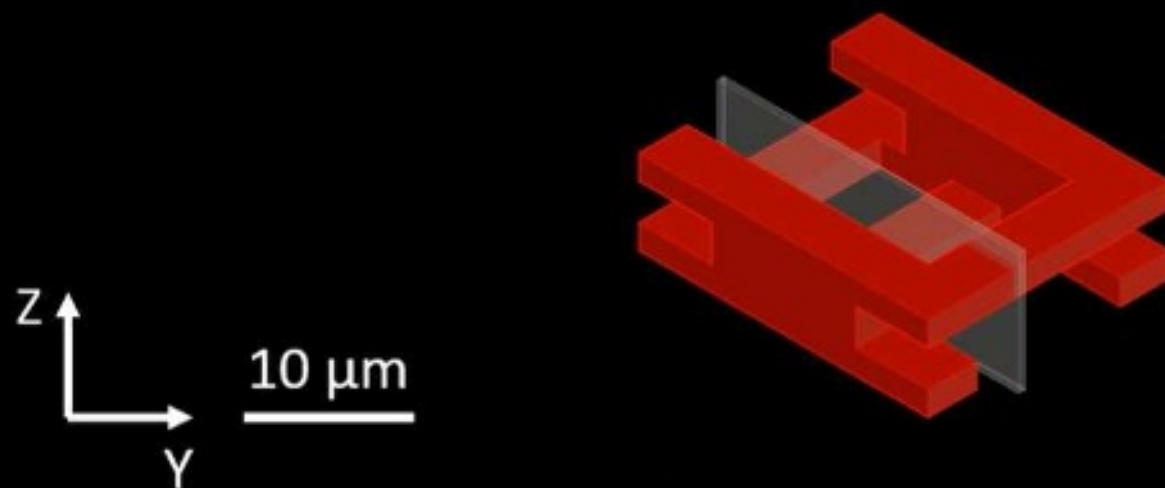
This is the author's peer reviewed, accepted manuscript. However, the online version of record will be different from this version once it has been copyedited and typeset.

PLEASE CITE THIS ARTICLE AS DOI:10.1063/5.0091615



Visualization 2

Lithography microstructure



Depth Retrieval

FOR Model
Depth Mapping